Research Square

Preprints are preliminary reports that have not undergone peer review.
They should not be considered conclusive, used to inform clinical practice,
or referenced by the media as validated information.

Stacking sequence effects on progressive intralaminar damage in open-hole auxetic and conventional hybrid composite laminates

Hossein Hosseini-Toudeshky
Amirkabir University of Technology (Tehran Polytechnic)
Sina Esmaeili Yengejeh
Amirkabir University of Technology (Tehran Polytechnic)
Azizollah Navaei
amirnava@aut.ac.ir

Amirkabir University of Technology (Tehran Polytechnic)

Article

Keywords: Hybrid composite laminates, Auxetic materials, Damage propagation, Poisson's ratio, Hashin failure criteria

Posted Date: November 5th, 2026

DOI: https://doi.org/10.21203/rs.3.rs-11330299/v1

License: This work is licensed under a Creative Commons Attribution 4.0 International License.
Read Full License

Additional Declarations: No competing interests reported.

Stacking sequence effects on progressive intralaminar damage in open-hole auxetic and conventional hybrid composite laminates

Hossein Hosseini-Toudeshky[1], Sina Esmaeili Yengejeh[1], and Azizollah Navaei[1*]

Department of Aerospace Engineering, Amirkabir University of Technology (Tehran Polytechnic), Hafez Ave, Tehran, Iran

*(Corresponding author E-mail: amirnava@aut.ac.ir)

Abstract

This study investigates damage initiation and progressive failure evolution in perforated hybrid composite laminates with engineered negative (auxetic) and positive Poisson's ratios through a combined experimental and numerical approach. To isolate the influence of laminate architecture, two hybrid laminates with identical constituent materials, nominal fiber volume fractions, and laminate thicknesses were fabricated while varying only the stacking sequence. Progressive damage evolution was simulated in ABAQUS using a Hashin-based failure model and validated against experimental open-hole tensile tests. The results show that auxetic laminates experience earlier matrix tensile damage initiation but exhibit a more gradual and spatially distributed damage evolution than conventional laminates. Consequently, damage localization around the hole is reduced, leading to improved stress redistribution and delayed structural degradation. Experimental results indicate that the auxetic laminate achieved approximately 7.5% higher load-carrying capacity and retained nearly 20% of its peak load after catastrophic failure, whereas the conventional laminate retained less than 10%. Layer-wise damage analysis further reveals that failure in auxetic laminates initiates within low- and intermediate-angle plies and propagates progressively through the laminate thickness, whereas conventional laminates exhibit rapid damage localization dominated by 90° plies. Overall, the results demonstrate the potential of auxetic layup architectures to improve damage tolerance, promote progressive failure, and enhance post-peak load-carrying capability in perforated hybrid composite laminates.

Keywords: Hybrid composite laminates, Auxetic materials, Damage propagation, Poisson’s ratio, Hashin failure criteria

Introduction

Fiber-reinforced polymer (FRP) composite laminates have become indispensable in lightweight engineering structures because of their high specific stiffness, excellent corrosion resistance, and superior design flexibility [1]. By tailoring the stacking sequence and fiber orientation, laminated composites provide engineers with a versatile approach to optimizing mechanical performance beyond the limitations of conventional isotropic materials [2]. Despite these advantages, practical

composite structures inevitably require holes and cut-outs for mechanical fastening, inspection, or assembly. These geometric discontinuities generate severe stress concentrations, which promote damage initiation, accelerate crack propagation, and significantly reduce the structural load-carrying capacity [3,4]. Consequently, understanding the interaction between laminate architecture, stress redistribution, and progressive damage evolution around stress concentrators remains one of the key challenges in the structural design of composite laminates.

Among the various design strategies proposed to improve the damage tolerance of perforated composites, hybridization has attracted considerable attention. Hybrid laminates combining carbon and glass fiber reinforcements have been widely investigated because they can effectively balance stiffness, strength, fracture toughness, and cost while improving resistance to damage accumulation and delamination [5,6]. Previous experimental and numerical studies have demonstrated that stacking sequence and ply thickness strongly influence crack initiation, fragmentation of low-elongation plies, interfacial delamination, and the interaction between fiber- and matrix-dominated failure mechanisms [7]. Furthermore, investigations under repeated and impact loading have shown that hybrid architectures can promote progressive stiffness degradation and redistribute damage more effectively than conventional laminates [8]. Energy-based damage models have also contributed to a better understanding of multidirectional failure mechanisms and progressive fracture behavior in hybrid composite systems [9].

In parallel with hybridization, tailoring the Poisson's ratio of laminated composites has emerged as another promising strategy for improving structural performance. Laminates with engineered negative Poisson's ratios (auxetic laminates) have attracted increasing attention because their transverse deformation behavior differs fundamentally from that of conventional composites. Analytical studies have demonstrated that appropriately designed angle-ply laminates can exhibit both in-plane and through-thickness negative Poisson's ratios, depending on fiber orientation and material anisotropy [10–12]. These theoretical predictions have subsequently been confirmed through experimental investigations, showing that both carbon/epoxy and hybrid composite laminates can achieve auxetic behavior solely through stacking sequence design without requiring specialized constituent materials [13]. Numerical studies have further demonstrated that fiber orientation, laminate architecture, and reinforcement type play important roles in controlling the auxetic response [14].

The unique deformation characteristics of auxetic laminates have been associated with several structural advantages. Previous investigations have reported enhanced buckling resistance resulting from auxetic-induced transverse strain redistribution rather than solely from changes in laminate stiffness [15,16]. Tensile characterization has also revealed the balance between stiffness reduction and the mechanical benefits associated with negative Poisson's ratio behavior [17]. Beyond quasi-static loading, auxetic laminates have demonstrated improved impact resistance and energy absorption, with numerical studies reporting reductions in fiber and matrix tensile damage under low-velocity impact loading [18–20]. Experimental studies on auxetic sandwich structures and cellular architectures have likewise shown superior specific energy absorption, while topology optimization and additive manufacturing have enabled the development of continuous-fiber auxetic configurations with enhanced mechanical performance [21–25]. Collectively, these studies indicate that auxetic laminate architectures can substantially influence stress transfer, deformation patterns, and damage evolution under various loading conditions.

Progressive damage modeling has become an indispensable tool for understanding failure evolution in composite laminates, particularly in structures containing stress concentrators. Finite element implementations based on failure criteria such as Hashin and Puck have been widely

employed to predict the initiation and propagation of fiber- and matrix-dominated damage while capturing the associated stiffness degradation during loading [20,26]. In addition, analytical and numerical studies incorporating progressive damage evolution have provided valuable insights into repeated loading, impact response, and structural durability of laminated composites [27,28]. Complementary experimental techniques, including digital image correlation (DIC) and embedded sensing, have further improved the understanding of strain localization and damage evolution by enabling full-field measurements for validating numerical predictions [29–32]. In our previous study [13], the auxetic and conventional hybrid layups considered here were designed and experimentally characterized using classical laminate theory, finite element analysis, and DIC. The measured Poisson's ratios and full-field strain distributions confirmed the negative and positive Poisson's ratio responses of the selected laminate configurations. Despite these advances, the damage behavior of perforated composite laminates remains highly complex because the presence of geometric discontinuities introduces localized stress concentrations and multiple interacting failure mechanisms. Previous studies have shown that tailoring the Poisson's ratio can reduce stress concentration around holes and alter crack initiation locations and propagation paths [3,13]. Likewise, investigations on perforated auxetic polymeric and fiber-reinforced structures have demonstrated improvements in stiffness and energy absorption that depend strongly on structural geometry [4]. However, most existing studies have primarily focused on global structural responses, such as peak load, stiffness, buckling performance, or absorbed energy, while comparatively limited attention has been given to the detailed sequence of ply-level damage initiation, progressive failure evolution, and post-peak load-carrying behavior in perforated hybrid laminates.

Although hybridization and auxetic laminate design have both demonstrated significant potential for improving composite structural performance, most previous investigations have focused on global mechanical responses, including Poisson's ratio, stiffness, peak strength, strain distribution, buckling resistance, impact mitigation, and energy absorption. Our previous study [13] established the design, fabrication, and experimental verification of perforated hybrid laminates with negative and positive Poisson's ratios. However, that investigation did not examine the ply-level sequence of damage initiation, the interaction between individual fiber- and matrix-dominated failure modes, progressive stiffness degradation, or post-peak failure evolution. Consequently, the influence of auxetic layup architecture on progressive damage mechanisms in perforated hybrid laminates remains insufficiently understood. Building upon the experimentally validated laminate configurations reported in Ref. [13], the present study investigates the progressive failure behavior of perforated hybrid composite laminates with engineered positive and negative Poisson's ratios. Two laminate configurations with identical constituent materials, laminate thickness, and nominal fiber volume fraction, but different stacking sequences, are considered to isolate the influence of laminate architecture on damage initiation and failure evolution. Unlike the previous study, which focused on layup design, Poisson's ratio, global stress–strain response, and strain distribution, the present work determines the required damage parameters and implements them in an ABAQUS finite element model employing a Hashin-based progressive damage formulation. Numerical predictions are then compared with experimental observations to evaluate the evolution of individual failure modes and validate the modeling framework. This complementary investigation provides a more comprehensive understanding of the mechanical response and failure mechanisms of perforated auxetic laminates, thereby contributing to the assessment of their potential applications in various engineering fields.

Experimental Characterization of Damage Parameters

Given the critical role and broad range of applications of composite materials, understanding and applying accurate damage criteria is essential for predicting structural performance. While experimental testing provides direct insights into material behavior, it is often costly and time consuming. Therefore, the use of numerical simulation methods particularly the finite element method (FEM) has become a practical and efficient alternative for reducing experimental efforts. Various failure and damage criteria for composite materials have been extensively developed and applied. The most commonly used criteria include the Maximum Stress, Maximum Strain, Tsai-Hill, Tsai-Wu, and Hashin models [33]. Among these, the Hashin failure criterion provides a more detailed classification of failure mechanisms in fiber-reinforced composites by distinguishing between four fundamental damage modes [34]:

1. Fiber tension failure
2. Fiber compression failure
3. Matrix tension failure
4. Matrix compression failure

These failure modes are represented in ABAQUS through the following output variables: HSNFTCRT, HSNFCCRT, HSNMTCRT, and HSNMCCRT, respectively. The Hashin failure model is implemented in ABAQUS as part of the Damage for Fiber-Reinforced Composites material model, allowing for progressive damage analysis under various loading conditions [35]. Due to its straightforward integration into Finite Element Method (FEM) simulations and Continuum Damage Mechanics (CDM) models, the Hashin criterion is extensively utilized in industrial applications [36]. Despite its advantages, the Hashin criterion has limitations, particularly in capturing delamination and other interlaminar failure mechanisms. Nevertheless, its ability to distinguish between fiber- and matrix-dominated failure modes makes it suitable for the present investigation of intralaminar damage. Given these limitations, future work may extend the present analysis by employing alternative approaches capable of capturing interlaminar damage and assessing its influence on failure progression. The following equations in Table1 encapsulate the Hashin failure criteria in a two-dimensional framework [34].

Table 1. Two-dimensional Hashin failure criteria

$$F_{ft} = \left(\frac{\sigma_{11}}{X_T}\right)^2 + \left(\frac{\sigma_{12}}{S_L}\right)^2 \leq 1 \qquad \sigma_{11} \geq 0 \qquad (1)$$

$$F_{fc} = \frac{\sigma_{11}}{-X_C} \leq 1 \qquad \sigma_{11} < 0 \qquad (2)$$

$$F_{mt} = \left(\frac{\sigma_{22}}{Y_T}\right)^2 + \left(\frac{\sigma_{12}}{S_L}\right)^2 \leq 1 \qquad \sigma_{22} \geq 0 \qquad (3)$$

$$F_{mc} = \left(\frac{\sigma_{22}}{2S_T}\right)^2 + \left[\left(\frac{Y_C}{2S_T}\right)^2 - 1\right]\frac{\sigma_{22}}{Y_C} + \left(\frac{\sigma_{12}}{S_L}\right)^2 \leq 1 \quad \sigma_{22} < 0 \tag{4}$$

Considering the assumption of a two-dimensional analysis, Equations (1) through (4) are utilized. The two-dimensional Hashin formulation was adopted because the specimens were thin laminates subjected predominantly to in-plane tensile loading, for which the plane-stress assumption provides an efficient representation of the principal intralaminar failure modes. Accordingly, the present analysis focuses on fiber- and matrix-dominated damage within individual plies. To implement these relations, it is crucial to introduce and subsequently determine the values of the relevant parameters. The key parameters are defined as follows:

X_T: Tensile strength in the fiber direction

X_C: Compressive strength in the fiber direction

Y_T: Tensile strength perpendicular to the fiber direction (matrix direction)

Y_C: Compressive strength perpendicular to the fiber direction (matrix direction)

S_T: Transverse shear strength

S_L: Longitudinal shear strength

Upon application of the Hashin failure criterion and identification of damage initiation within an element, the matrix stiffness degradation components are computed based on fracture energy values, the coefficient α which quantifies the contribution of shear stress to the onset of fiber tensile failure and the longitudinal strain. These degradation components are represented by d_I, where the subscript I corresponds to the four failure modes of the fiber and matrix under tension and compression. When any of these degradation components reach a value of unity, the elastic modulus of the affected element is reduced to zero, leading to a degradation in the overall laminate properties. This progressive stiffness degradation results in a nonlinear stress-strain behavior of the laminate. After the maximum sustainable stress is reached, the descending branch of the stress-strain curve decreases linearly, as outlined in reference [36]. The following section presents a detailed discussion on the parameter extraction methods. For precise simulation of hybrid laminates with both positive and negative Poisson's ratios, the material properties of the constituents are essential. Thus, in addition to the mechanical properties of unidirectional carbon/epoxy and glass/epoxy laminates, damage parameters including the strengths previously introduced must be determined. The methodology for extracting these parameters is provided in the subsequent section.

Extraction of Damage Parameters

For the implementation of the two-dimensional Hashin failure criterion in ABAQUS, it is essential to determine 16 parameters for each composite material. Consequently, a total of 32 mechanical and damage parameters must be extracted for the two materials, carbon/epoxy and glass/epoxy. To evaluate the necessary material properties, standard laminates are fabricated using the Vacuum-

Assisted Resin Transfer Molding (VARTM) process. This method is employed to measure Young's modulus both along the fiber direction and in the transverse direction [13]. The corresponding values are summarized in Table 2. To determine the ultimate tensile and compressive strengths along and transverse to the fiber direction, standard specimens are manufactured and tested according to ASTM D3039 and ASTM D3410 standards.(Figure1) Specifically, eight-layer 90° specimens are used to measure tensile strength transverse to the fibers (YT), eight-layer 0° specimens for compressive strength along the fibers (XC), four-layer 90° specimens for compressive strength transverse to the fibers (YC), and four-layer 0° specimens for tensile strength along the fibers (XT). The fiber volume fraction in the specimens was maintained at approximately 43%. This value was determined using the burn-off method described in our previous study [13]. A portion of the laminate was weighed before and after removing the epoxy matrix in a furnace. The fiber volume fraction was then calculated using the measured fiber and matrix masses together with their corresponding densities. The standard specimens described above are shown in Figure 1.

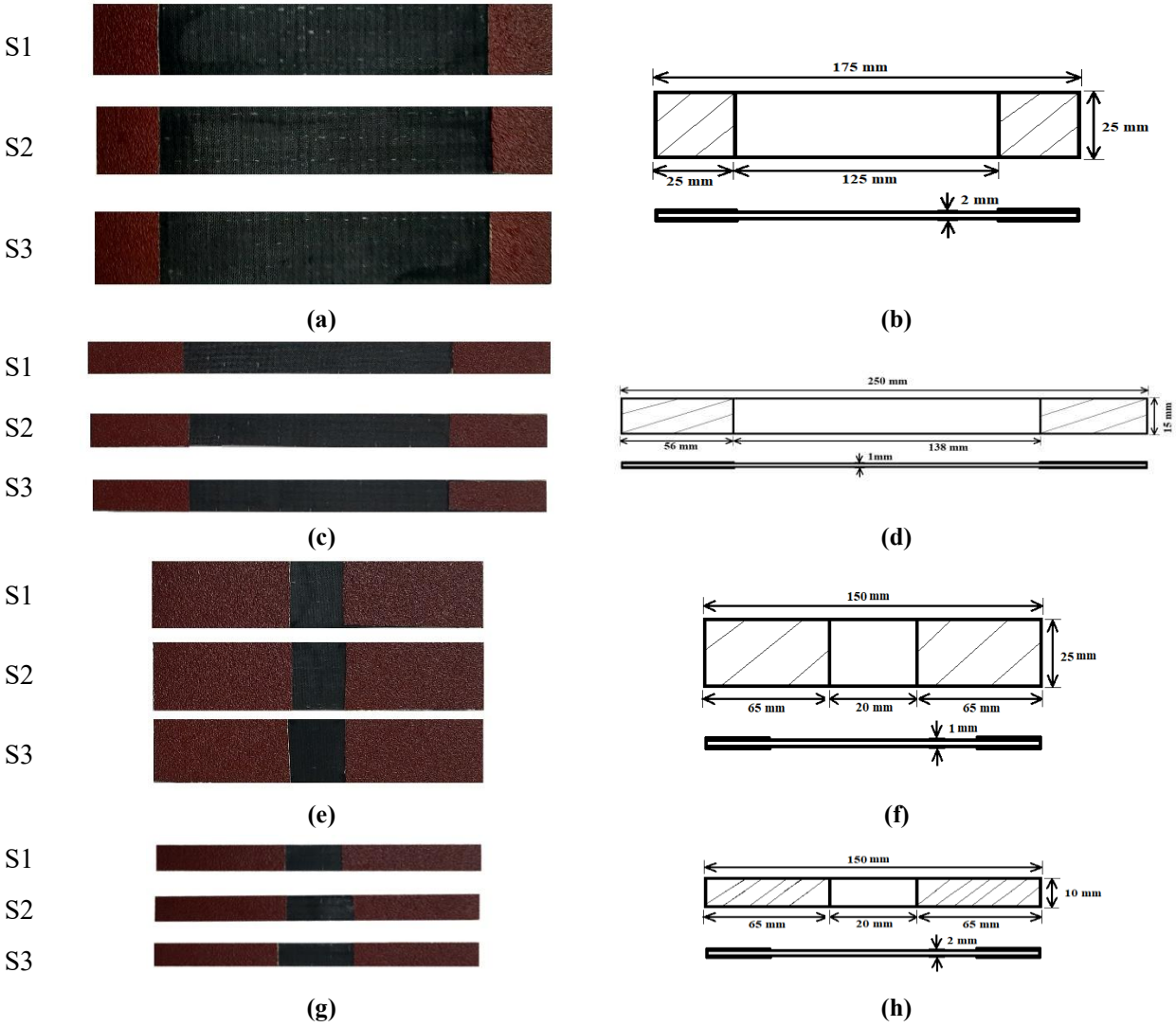


Figure 1: Specimens manufactured according to ASTM-D3039 standards
(a) CFRP specimens for Y_T, (b) Laminate dimensions for Y_T
(c) CFRP specimens for X_T, (d) Laminate dimensions for X_T
(e) CFRP specimens for Y_C, (f) Laminate dimensions for Y_C
(g) CFRP specimens for X_C, (h) Laminate dimensions for X_C

The values obtained from these tests are presented in Table 2.

Table 2: Experimental Test Results and Outputs for Carbon/Epoxy

Parameter	Unit	Sample 1	Sample 2	Sample 3	Average	Standard Deviation
Longitudinal Elastic Modulus (E1)	GPa	109.5	96.8	101.3	102.53	6.44
Maximum Tensile Strength along the Fiber Direction (XT)	MPa	992.27	1068.61	996.14	1019.01	43
Lateral Elastic Modulus (E2)	GPa	6.10	5.80	5.65	5.85	0.23
Maximum Tensile Strength perpendicular to the Fiber Direction (YT)	MPa	163.5	212	202.9	192.8	25.78
Maximum Compressive Strength along the Fiber Direction (XC)	MPa	337.74	426.76	358.21	374.24	46.62
Maximum Compressive Strength perpendicular to the Fiber Direction (YC)	MPa	288.8	361.4	227.8	292.7	66.88

Based on the results presented in Table 2, fifteen additional parameters for the glass/epoxy material were estimated using the Rule of Mixtures and the Halpin–Tsai micromechanical model, as appropriate. The Rule of Mixtures was used to estimate properties based on the volume fractions and constituent properties of the fibers and matrix [38], while the Halpin–Tsai model was applied to estimate the transverse and shear properties of the composite [39]. The four fracture energy parameters were determined by calculating the area under the stress–displacement curves from damage initiation to final failure, following the approach described in Ref. [7]. To ensure consistency with the ABAQUS damage evolution model, the extracted values were used as fracture energy inputs, as illustrated in Figure 2.The observed scatter in tensile and compressive strength values in the longitudinal and transverse directions may be attributed to variations in fiber-resin distribution, microscopic voids, specimen preparation, and testing conditions.

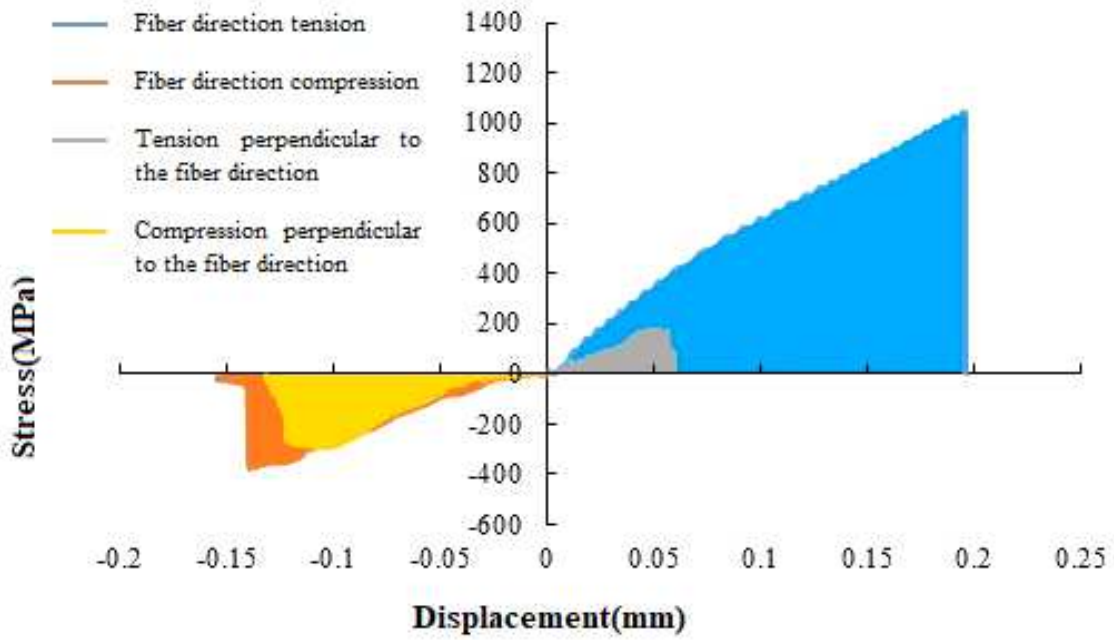


Figure 2: Stress-Displacement Curves of Standard Carbon/Epoxy Specimens for Determination of Fracture Energy Values

The area of the specified regions in Figure 2 was calculated using the trapz function in MATLAB. The resulting fracture energy values are as follows:

- Longitudinal tensile fracture energy (Gft): 112.5 N/mm
- Longitudinal compressive fracture energy (G_{fc}): 25.81 N/mm
- Transverse tensile fracture energy (G_{mt}): 1.8 N/mm
- Transverse compressive fracture energy (G_{mc}): 17.16 N/mm

Therefore, in this study, a total of 19 parameters were obtained directly through experimental testing or analysis of test results. Table 3 summarizes the extraction methods for all parameters related to both materials used in this research. In general, three specimens were fabricated and tested to determine the parameters obtained through standard specimen fabrication and experimental testing. As detailed in Ref. [13], three perforated specimens were tested for the conventional (non-auxetic) laminate, whereas a single specimen with the specific auxetic configuration was fabricated and tested due to its distinctive architecture. Since the specimen fabrication procedures and configurations were described in detail in the previous study, the present work focuses on the experimental results and their analysis.

Table 3: Methods for Extracting Parameters Required for Implementing the Hashin Criterion in ABAQUS

Property	Symbol	Unit	Material	Value	Description
	E1	GPa	Carbon/Epoxy	102.53	Extracted from experimental test

Longitudinal Elastic Modulus			Glass/Epoxy	25.171	Extracted from experimental test and mixing law
Lateral Elastic Modulus	E2	GPa	Carbon/Epoxy	5.85	Extracted from experimental test
			Glass/Epoxy	4.983	Extracted from experimental test and mixing law
In-Plane Shear Modulus	G12	GPa	Carbon/Epoxy	2.483	Extracted from experimental test and Halpin-Tsai equation
			Glass/Epoxy	1.887	Extracted from experimental test and Halpin-Tsai equation
Out-of-Plane Shear Modulus	G13	GPa	Carbon/Epoxy	2.483	Extracted from experimental test and Halpin-Tsai equation
			Glass/Epoxy	1.887	Extracted from experimental test and Halpin-Tsai equation
Out-of-Plane Shear Modulus	G23	GPa	Carbon/Epoxy	2.52	From Ref. [37]
			Glass/Epoxy	3.31	From Ref. [37]
Poisson's Ratio	-	-	Carbon/Epoxy	0.334	Extracted from experimental test and mixing law
			Glass/Epoxy	0.324	Extracted from experimental test and mixing law
Tensile Strength along Fiber	XT	MPa	Carbon/Epoxy	1019	Extracted from experimental test
			Glass/Epoxy	460	From reference [37]
Compressive Strength along Fiber	XC	MPa	Carbon/Epoxy	374.2	Extracted from experimental test
			Glass/Epoxy	275	From Ref. [37]
Tensile Strength perpendicular to Fiber	YT	MPa	Carbon/Epoxy	192.8	Extracted from experimental test
			Glass/Epoxy	147	From Ref. [37]
Compressive Strength perpendicular to Fiber	YC	MPa	Carbon/Epoxy	292.7	Extracted from experimental test
			Glass/Epoxy	200	From Ref. [37]
Longitudinal Shear Strength	SL	MPa	Carbon/Epoxy	51	From Ref. [37]
			Glass/Epoxy	45	From Ref. [37]
Transverse Shear Strength	ST	MPa	Carbon/Epoxy	146.3	Using equations (half Yc)
			Glass/Epoxy	100	Using equations (half Yc) [38]
Tensile Fracture Energy along Fiber	Gft	N/mm	Carbon/Epoxy	112.5	Extracted from experimental test results
			Glass/Epoxy	32	From Ref. [37]
Compressive Fracture Energy along Fiber	Gfc	N/mm	Carbon/Epoxy	25.81	Extracted from experimental test results
			Glass/Epoxy	20	From Ref. [37]
Tensile Fracture Energy in Lateral Direction	Gmt	N/mm	Carbon/Epoxy	1.8	Extracted from experimental test results
			Glass/Epoxy	4.5	From Ref. [37]
Compressive Fracture Energy in Lateral Direction	Gmc	N/mm	Carbon/Epoxy	17.16	Extracted from experimental test results
			Glass/Epoxy	4.5	From Ref. [37]

Damage Modeling Using the FEM Approach

The eight-ply auxetic and conventional hybrid laminate configurations employed in the present study were previously designed, fabricated, and experimentally characterized in Ref. [13]. The present work adopts these validated configurations and extends the previous investigation by focusing on damage initiation, progressive stiffness degradation, and ply-level failure evolution. The auxetic laminate had the stacking sequence [10/80/10/70/70/10/80/10], whereas the conventional laminate had the stacking sequence [10/45/−45/90/90/−45/45/10]. Both configurations used the same carbon/glass material arrangement and were symmetric about the laminate mid-plane. The experimentally measured Poisson's ratio was approximately −0.16 for

the auxetic laminate and approximately +0.15 for the conventional laminate [13]. Table 4 summarizes the key specifications of the eight-layer hybrid laminates.

Table 4: Mechanical properties and Poisson's ratio of the auxetic and conventional hybrid laminates

Specimen		Poisson's Ratio			E1 (GPa)		
Type of Laminates	number	Experimental	FEM	Theoretical	Experimental	FEM	Theoretical
Hybrid 1 [10/80/10/70/70/10/80/10] [C C G C C G C C]	1	-0.152	-0.159	-0.160	31.28	27.49	27.48
	2	-0.167			28.52		
Hybrid 2 [10/45/-45/90/90/-45/45/10] [C C G C C G C C]	1	0.136	0.152	0.156	27.015	27.63	27.71
	2	0.235			27.052		
	3	0.165			27.076		

In the finite element modeling (FEM), the specimen is simulated as a 3D deformable shell (planar shell model). Shell elements were employed because the laminate thickness was much smaller than its in-plane dimensions. They provide an efficient and accurate representation of the global tensile response and in-plane stress–strain distribution of laminated composites while significantly reducing the computational cost compared with three-dimensional solid elements. The mechanical properties and damage parameters for both glass/epoxy and carbon/epoxy materials, as listed in Table 3, are assigned within the software. In the Composite Layup module, the laminate configuration (including layer thickness, orientation, and material type) is defined, and the appropriate coordinate system is specified. Since both positive and negative Poisson's ratio laminates are modeled, all simulation steps are identical for both types, with the only difference being the stacking angles assigned to each layer. Furthermore, because both laminate configurations have the same constituent materials and fiber-to-matrix volume fraction, the constituent-level material properties are identical, and the only difference between the models is the stacking sequence. In the Step module, the solution increment is set to 0.01, and the output variables corresponding to Hashin failure modes are selected. These outputs include all fiber and matrix failure types under both tensile and compressive loading conditions. For plotting the force–displacement curves, two edges of the specimen are defined as sets, from which longitudinal displacement and reaction force outputs are extracted. In the Load module, one end of the specimen is fully constrained, while the opposite end is subjected to a displacement of 6 mm for the auxetic hybrid laminate and 4.5 mm for the non-auxetic hybrid laminate. To ensure the accuracy of the simulation results and mesh independence, element settings are configured initially. In this regard, Quad- Structured shell elements are used, and the Element Deletion feature is activated to facilitate progressive failure modeling. The adopted progressive damage formulation was further assessed by comparing the predicted damage patterns and fracture morphology with the corresponding experimental observations. This comparison provides a qualitative validation of the model's capability to capture the dominant intralaminar failure mechanisms in both auxetic and conventional laminates.

Mesh Independence Study

Upon finalizing all simulation settings and parameters, analyses were performed on models with different element densities. To evaluate mesh independence, the maximum reaction force recorded at the predefined set was analyzed in relation to the number of elements. The results of this evaluation are presented in the following table and graph. For the mesh convergence study, nodal displacements were first extracted and averaged. For the reaction force, the total force exerted on all elements located in the support region was calculated. Subsequently, a force–displacement curve was generated using these data. The peak load obtained from this curve was recorded and used to complete Table 5, based on the observed results.

Table 5: Mesh Independence Study for the Perforated Auxetic Hybrid Laminate Based on Maximum Reaction Force

Model Name	Number of Elements	Maximum Reaction Force (RF) (N)
M1	1040	13185.05
M2	1990	13501.38
M3	6088	13849.24
M4	10800	14244.03
M5	28000	14317.99
M6	44800	14388.24
M7	56000	14390.24

The corresponding plot is shown in Figure 3.

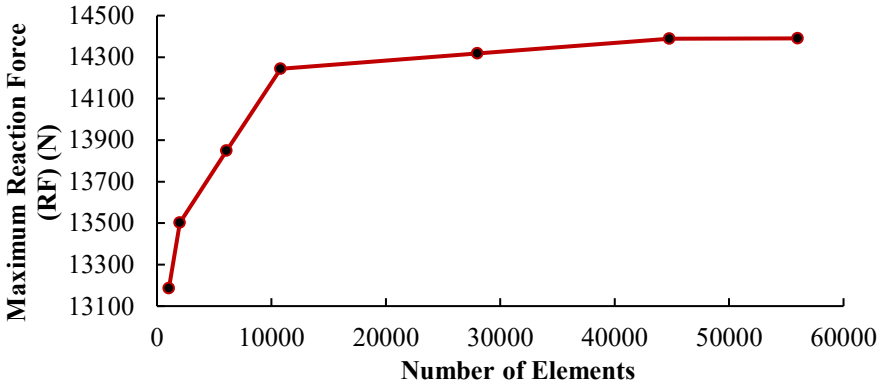
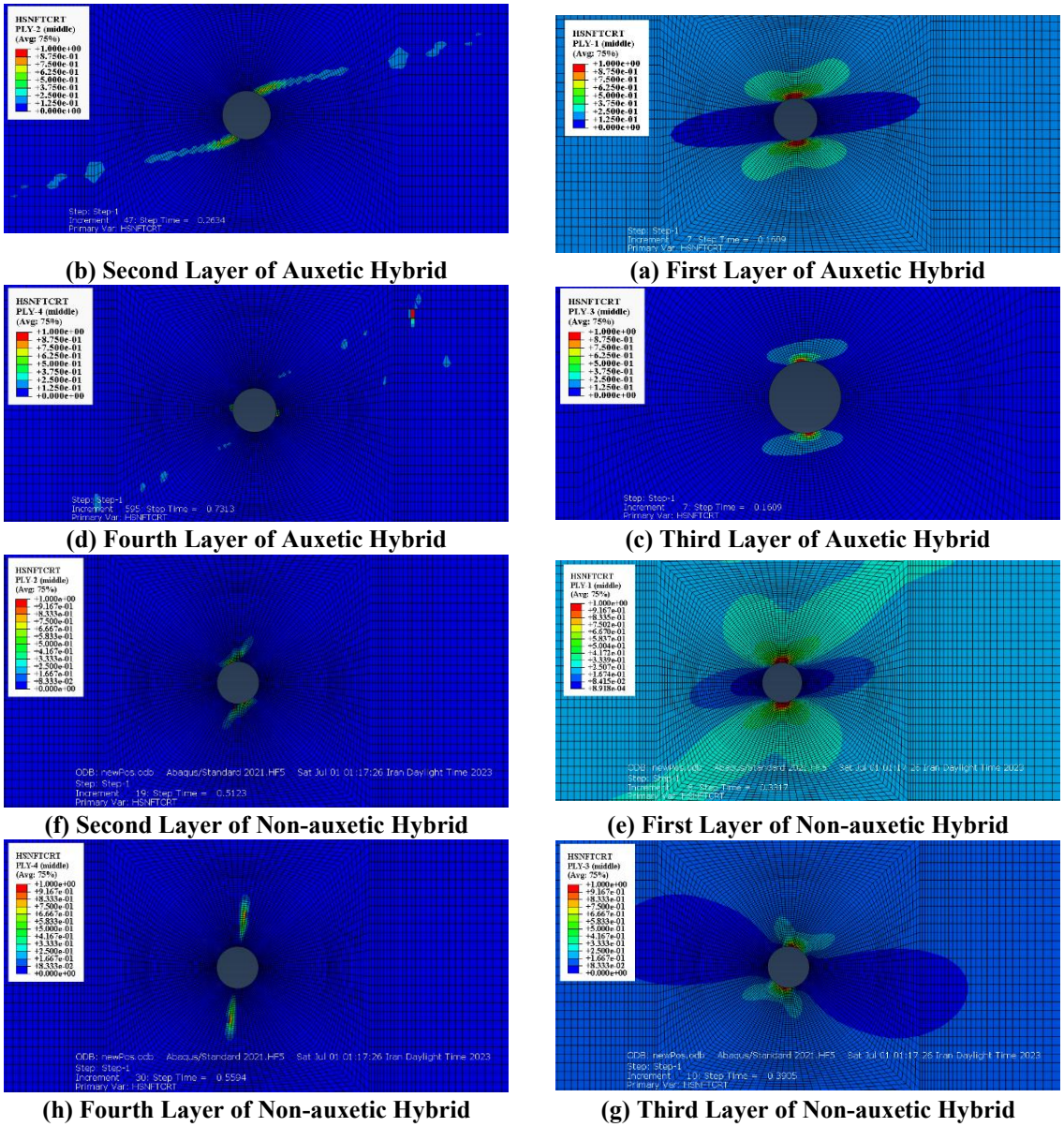


Figure 3: Mesh Independence Analysis for the Perforated Auxetic Hybrid Laminate Based on the Maximum Reaction Force

The relative difference between the selected mesh (10,800 elements) and the most refined mesh (56,000 elements) was approximately 1%, confirming acceptable convergence for engineering purposes. Considering the balance between computational cost and accuracy, a mesh containing 10,800 elements was selected for subsequent analyses, as further refinement resulted in only marginal improvements in peak load prediction. It is important to note that the plot in Figure 3 corresponds to the perforated auxetic hybrid laminate.

Damage Analysis of Layers and Comparison with Experimental Tests

Upon completing the analyses for both perforated hybrid laminates with negative and positive Poisson's ratios, several outputs are examined. These outputs include the initiation and progression of damage across all layers, evaluated using four distinct Hashin failure modes, the evolution of the load–displacement curves, and the stress–strain behavior of the laminates. Initially, the results related to the four Hashin failure modes are presented. Figures 4 through 11 depict, respectively, the initiation and progression of the failure modes HSNFTCRT, HSNFCCRT, HSNMTCRT, and HSNMCCRT for both auxetic and positive Poisson's ratio laminates. Given the symmetry of the eight-layer hybrid laminates, these results are presented for only the upper half of the laminate (layers 1 to 4).



(b) Second Layer of Auxetic Hybrid **(a) First Layer of Auxetic Hybrid**

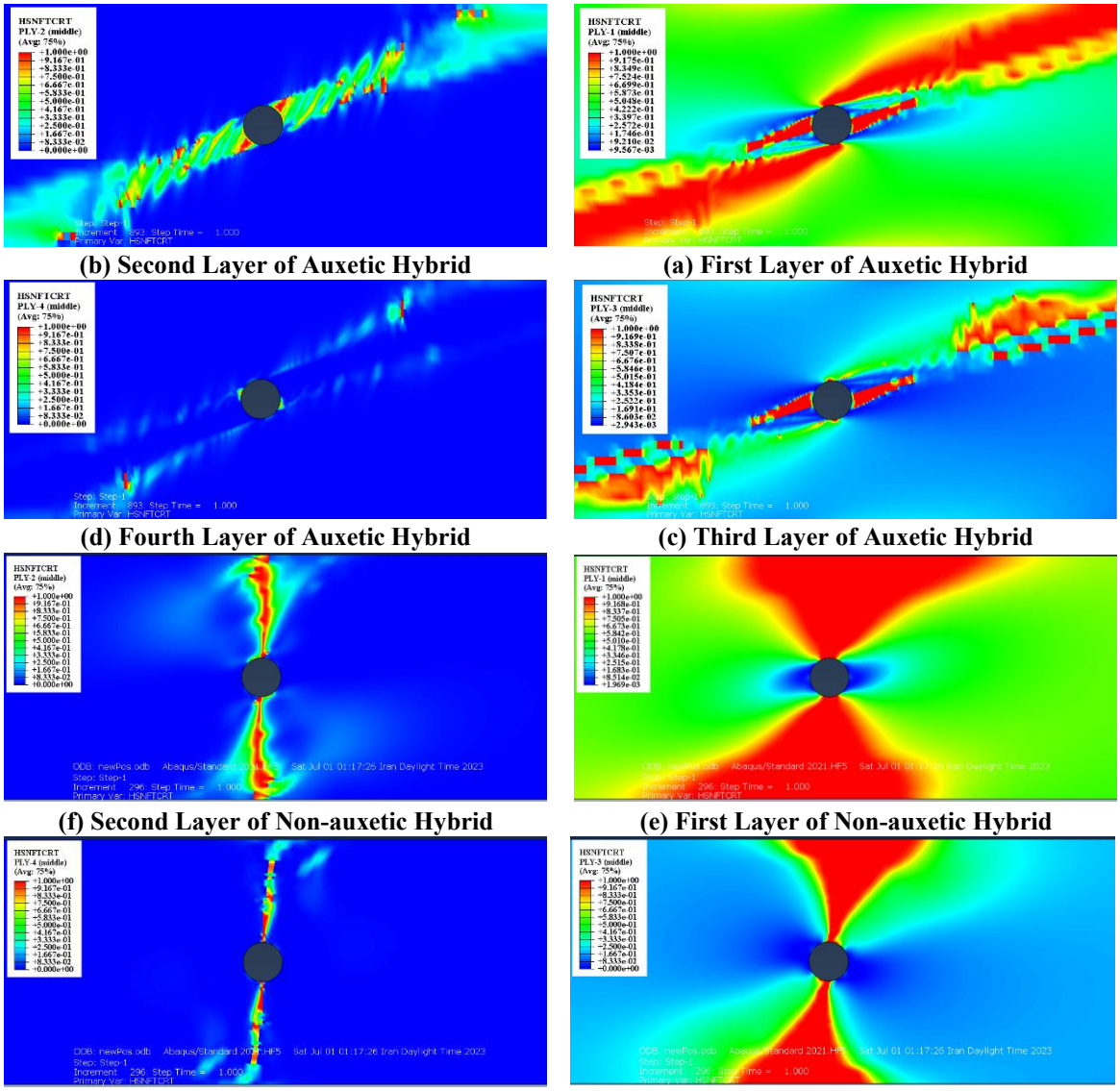
(d) Fourth Layer of Auxetic Hybrid **(c) Third Layer of Auxetic Hybrid**

(f) Second Layer of Non-auxetic Hybrid **(e) First Layer of Non-auxetic Hybrid**

(h) Fourth Layer of Non-auxetic Hybrid **(g) Third Layer of Non-auxetic Hybrid**

Figure 4: Damage Initiation in Fiber Tensile Failure Mode (HSNFTCRT)

In Figure 4, the initiation of damage in the fiber tensile failure mode (HSNFTCRT) is depicted for both auxetic and positive Poisson's ratio laminates. The results reveal that in both laminate types, the first and third layers initiate damage at earlier stages and under lower loads compared to the other layers. Furthermore, the location of damage initiation for all layers in both auxetic and positive Poisson's ratio laminates originates from the region around the hole.



(b) Second Layer of Auxetic Hybrid **(a) First Layer of Auxetic Hybrid**

(d) Fourth Layer of Auxetic Hybrid **(c) Third Layer of Auxetic Hybrid**

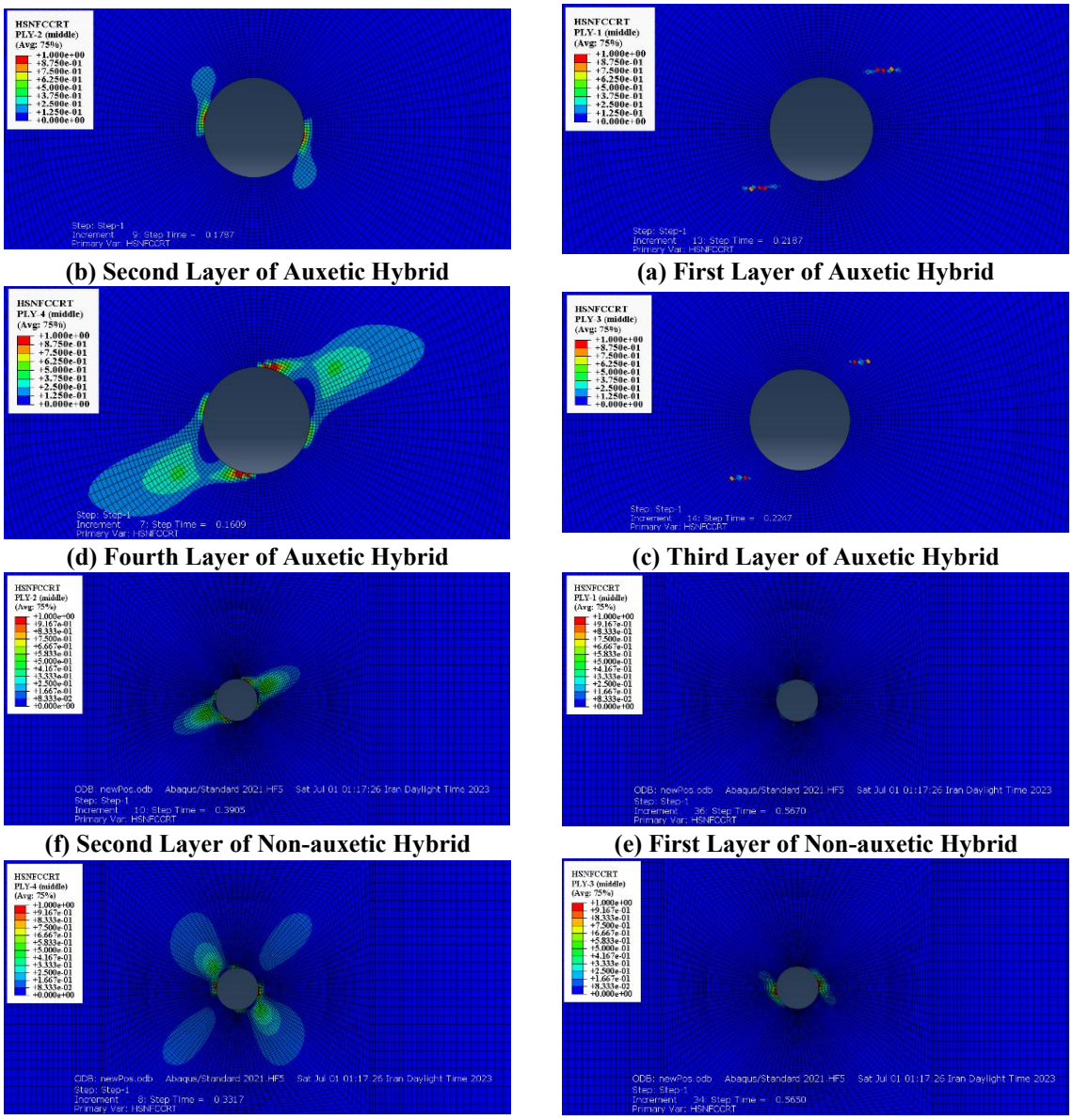
(f) Second Layer of Non-auxetic Hybrid **(e) First Layer of Non-auxetic Hybrid**

(h) Fourth Layer of Non-auxetic Hybrid **(g) Third Layer of Non-auxetic Hybrid**

Figure 5: Damage Propagation in Fiber Tensile Failure Mode (HSNFTCRT)

Figure 5 illustrates the final damage propagation in the fiber tensile failure mode (HSNFTCRT) across all layers of both auxetic and non-auxetic hybrid composites. The results indicate that the extent of damage propagation is greatest in the first and third layers, where damage initiation was previously observed. Furthermore, the results show that the layers with damage initiation occurring

near the hole exhibit a higher intensity and faster rate of damage propagation compared to the other layers.



(b) Second Layer of Auxetic Hybrid **(a) First Layer of Auxetic Hybrid**

(d) Fourth Layer of Auxetic Hybrid **(c) Third Layer of Auxetic Hybrid**

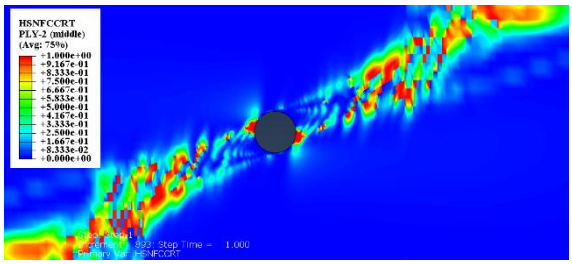
(f) Second Layer of Non-auxetic Hybrid **(e) First Layer of Non-auxetic Hybrid**

(h) Fourth Layer of Non-auxetic Hybrid **(g) Third Layer of Non-auxetic Hybrid**

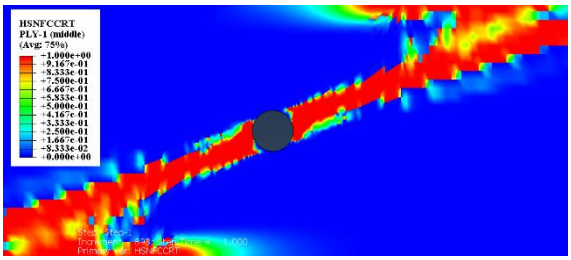
Figure 6: Damage Initiation in Fiber Compressive Failure Mode (HSNFCCRT)

In Figure 6, the initiation of damage in the fiber compressive failure mode (HSNFCCRT) is shown for both auxetic and positive Poisson's ratio laminates. By comparing the onset of failure in both fiber failure modes, it can be concluded that the HSNFCCRT mode initiates at a later stage and under higher load. Given the overall tensile loading condition applied to the laminates, the fiber compressive failure mode is activated locally due to stress redistribution around the hole. This observation is physically consistent with the stress redistribution mechanism around the hole. Examining the fiber orientation angle of each layer reveals that the closer the layer's angle is to 90 degrees, the earlier the failure mode initiates and at a lower load. Furthermore, the analysis of

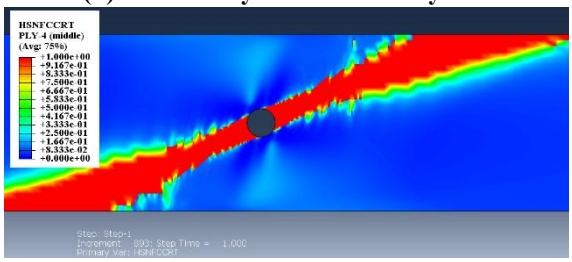
damage propagation in the same failure mode, shown in Figure 7, indicates that layers with fiber angles near 45 degrees exhibit more intense damage propagation compared to the other layers.



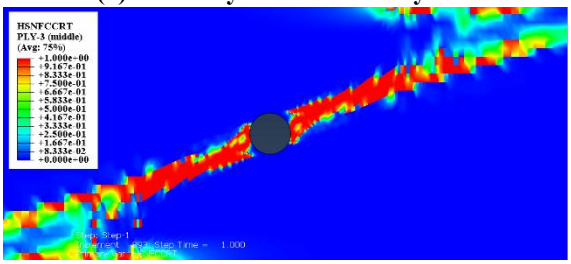
(b) Second Layer of Auxetic Hybrid



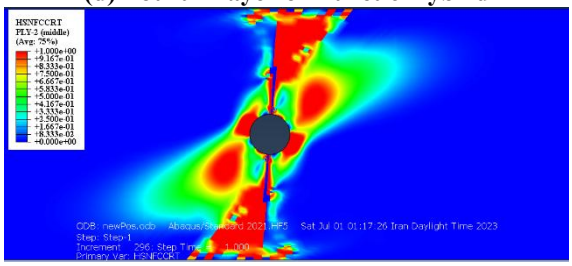
(a) First Layer of Auxetic Hybrid



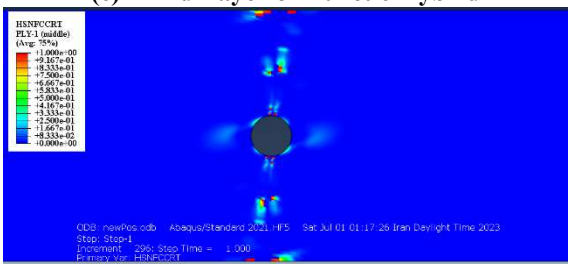
(d) Fourth Layer of Auxetic Hybrid



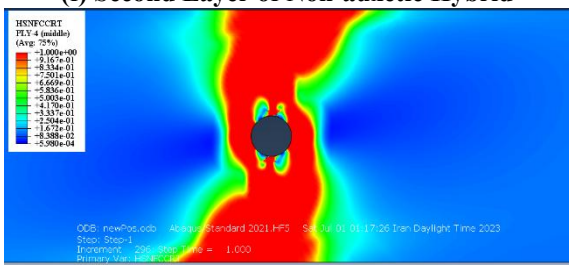
(c) Third Layer of Auxetic Hybrid



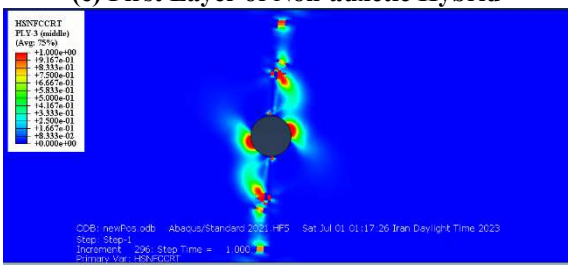
(f) Second Layer of Non-auxetic Hybrid



(e) First Layer of Non-auxetic Hybrid

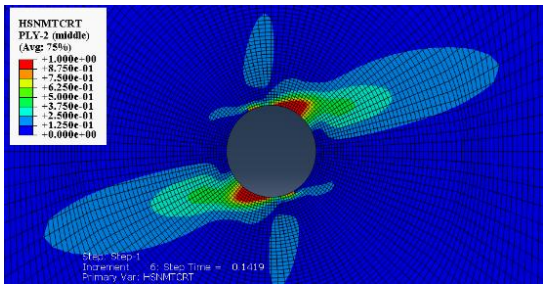


(h) Fourth Layer of Non-auxetic Hybrid

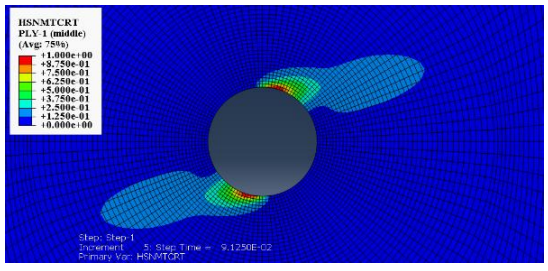


(g) Third Layer of Non-auxetic Hybrid

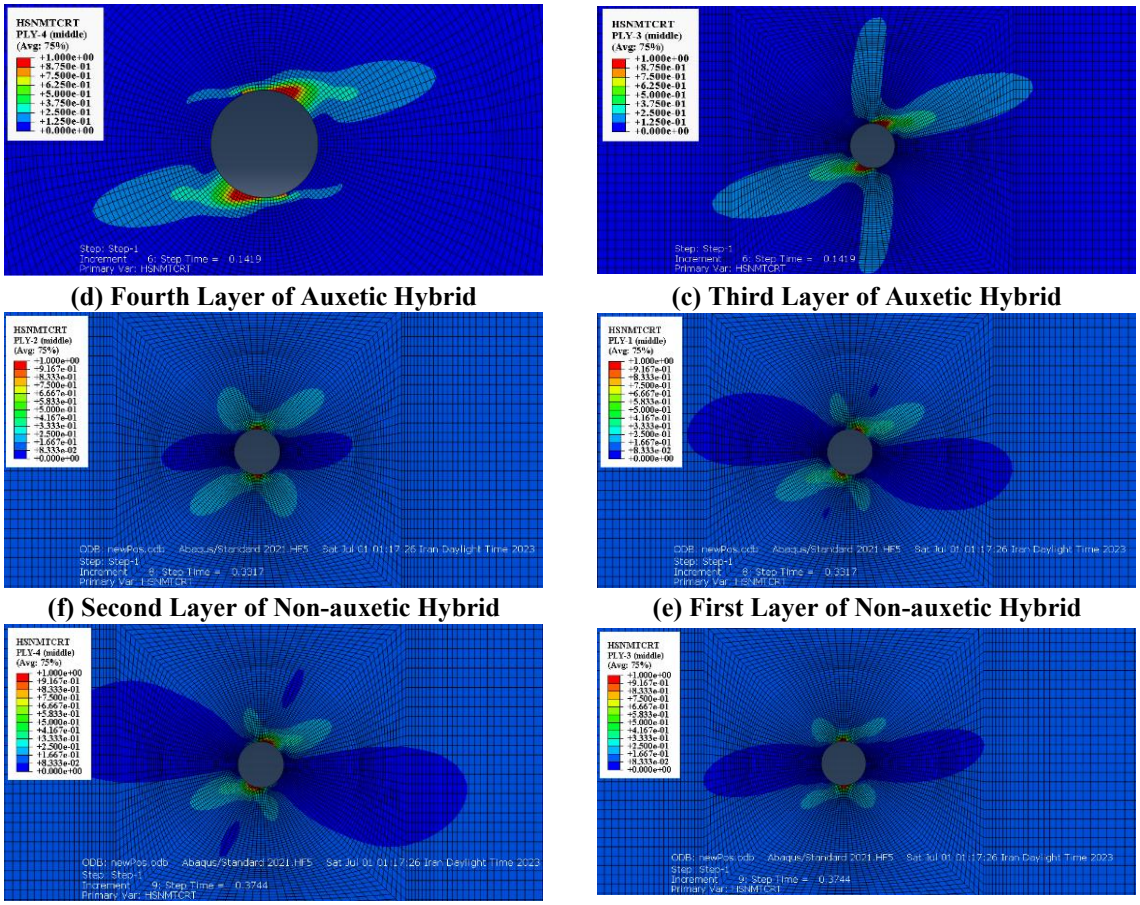
Figure 7: Damage Propagation in Fiber Compressive Failure Mode (HSNFCCRT)



(b) Second Layer of Auxetic Hybrid



(a) First Layer of Auxetic Hybrid



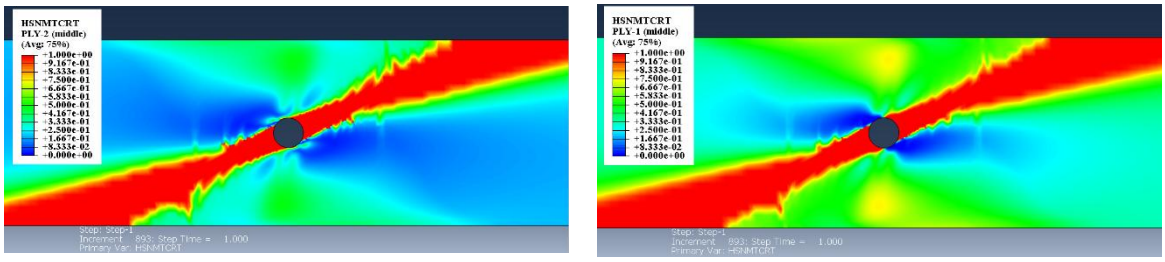
(d) Fourth Layer of Auxetic Hybrid **(c) Third Layer of Auxetic Hybrid**

(f) Second Layer of Non-auxetic Hybrid **(e) First Layer of Non-auxetic Hybrid**

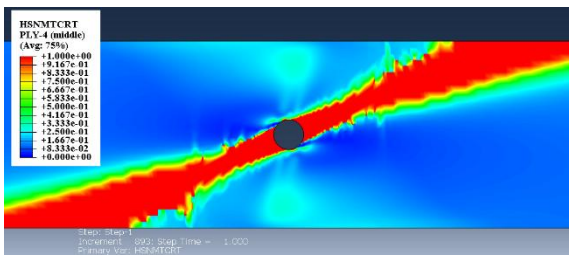
(h) Fourth Layer of Non-auxetic Hybrid **(g) Third Layer of Non-auxetic Hybrid**

Figure 8: Damage Initiation in Matrix Tensile Failure Mode (HSNMTCRT)

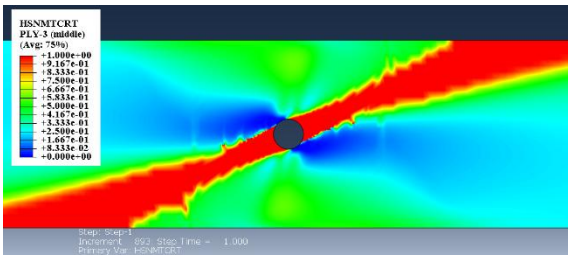
Figure 8 shows the initiation of matrix tensile damage in the two laminates. In the auxetic laminate, matrix tensile damage first initiates in layer 1 at a displacement of 0.54 mm and subsequently develops in plies 2–4 at approximately 0.85 mm. In the conventional laminate, the corresponding damage mode initiates in plies 1 and 2 at approximately 0.99 mm and then appears in plies 3 and 4 at approximately 1.12 mm. Because the step variable represents normalized analysis time rather than physical test time, the damage-onset values are reported primarily in terms of applied displacement.



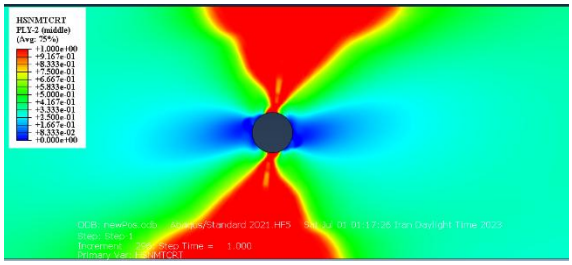
(b) Second Layer of Auxetic Hybrid **(a) First Layer of Auxetic Hybrid**



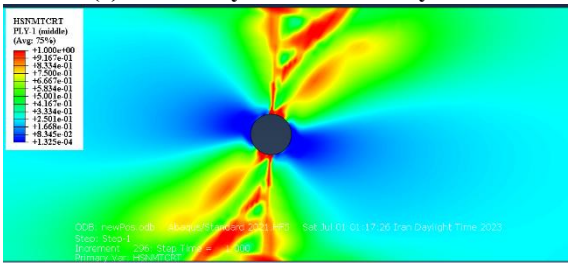
(d) Fourth Layer of Auxetic Hybrid



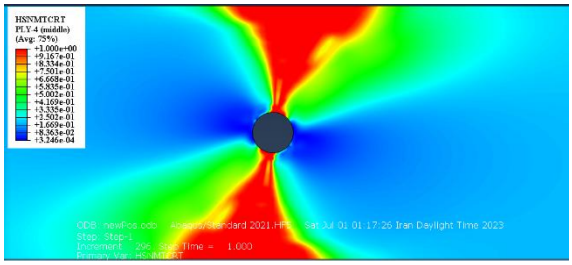
(c) Third Layer of Auxetic Hybrid



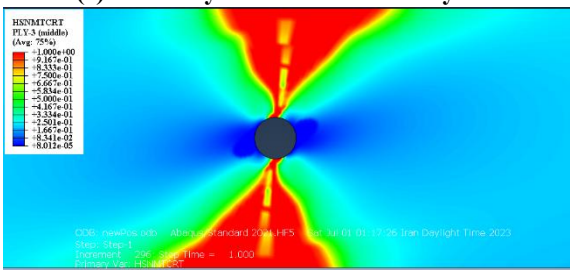
(f) Second Layer of Non-auxetic Hybrid



(e) First Layer of Non-auxetic Hybrid



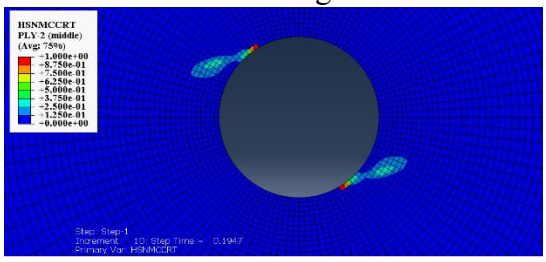
(h) Fourth Layer of Non-auxetic Hybrid



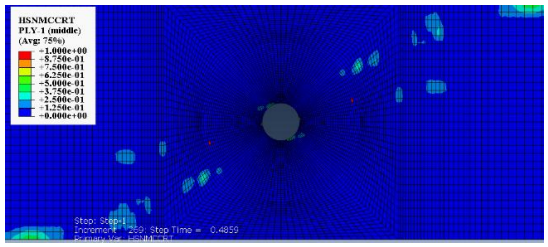
(g) Third Layer of Non-auxetic Hybrid

Figure 9: Damage Propagation in Matrix Tensile Failure Mode (HSNMTCRT)

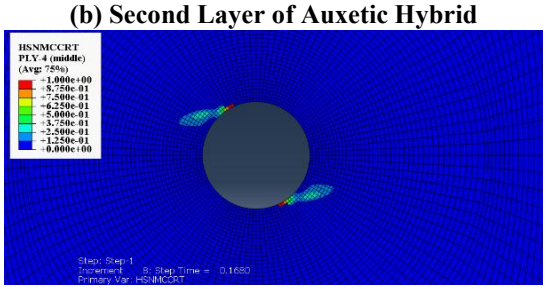
In the HSNMTCRT failure mode, all layers containing carbon and glass fibers in both auxetic and positive Poisson's ratio laminates experience damage. Considering that, during tensile loading of the laminates, the majority of the load is carried by the fibers, it is expected that the matrix under tension would undergo the most significant damage. Figure 9 clearly demonstrates the dominant role of matrix tensile cracking in the overall damage evolution process.



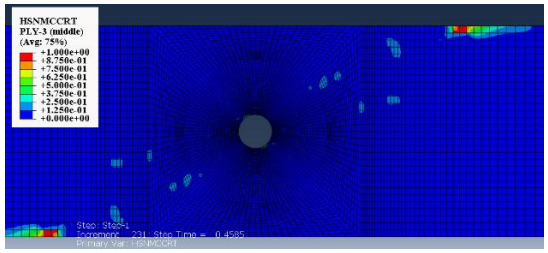
(b) Second Layer of Auxetic Hybrid



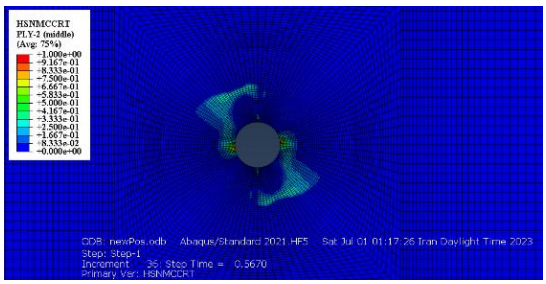
(a) First Layer of Auxetic Hybrid



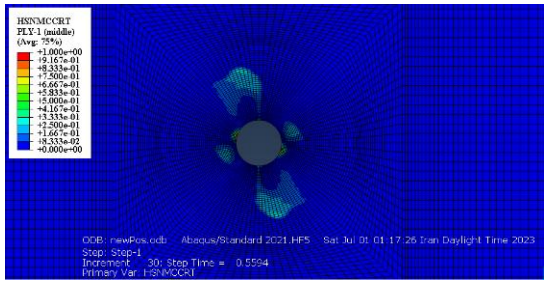
(d) Fourth Layer of Auxetic Hybrid



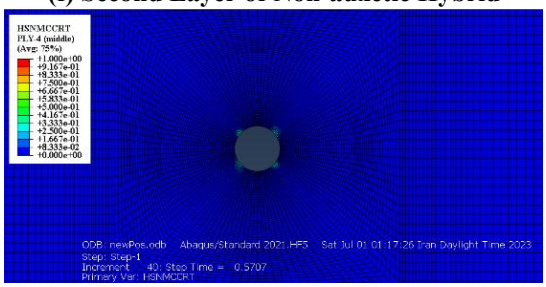
(c) Third Layer of Auxetic Hybrid



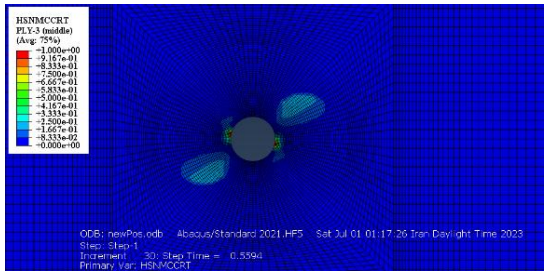
(f) Second Layer of Non-auxetic Hybrid



(e) First Layer of Non-auxetic Hybrid



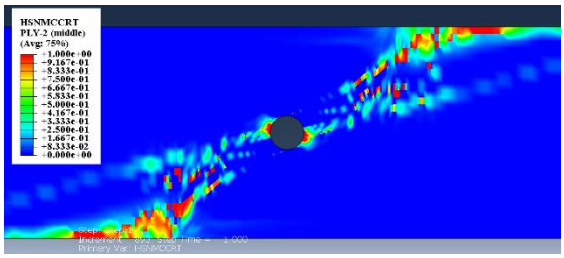
(h) Fourth Layer of Non-auxetic Hybrid



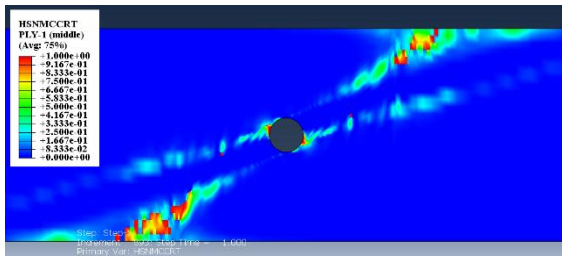
(g) Third Layer of Non-auxetic Hybrid

Figure 10: Damage Initiation in Matrix Compressive Failure Mode (HSNMCCRT)

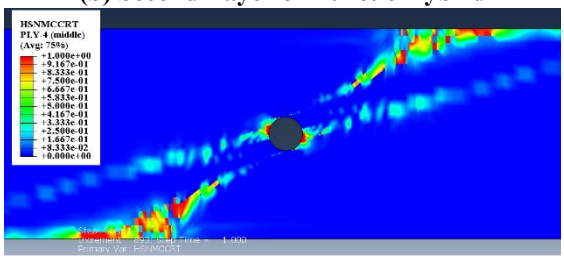
In Figure 10, the initiation of damage in the matrix compressive failure mode is shown for both auxetic and positive Poisson's ratio laminates. Given the type of loading applied, the onset of failure in this mode occurs later compared to other failure modes. As shown in Figure 11, the propagation of damage in the HSNMCCRT mode is also less severe than in the other failure modes.



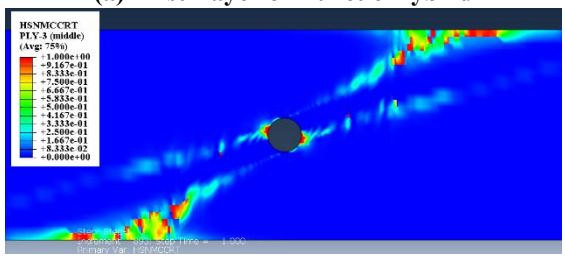
(b) Second Layer of Auxetic Hybrid



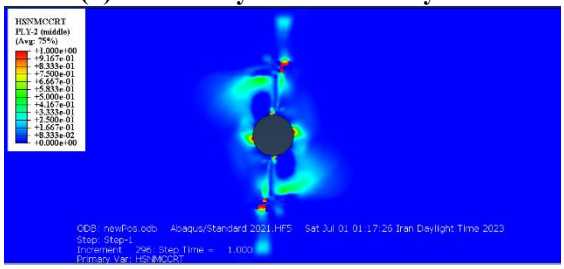
(a) First Layer of Auxetic Hybrid

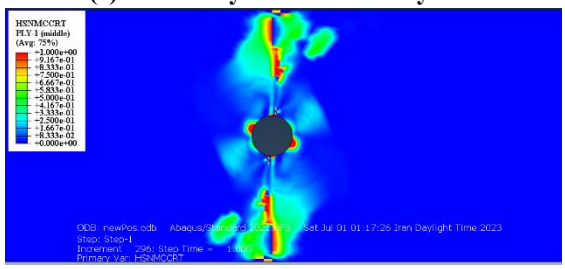


(d) Fourth Layer of Auxetic Hybrid

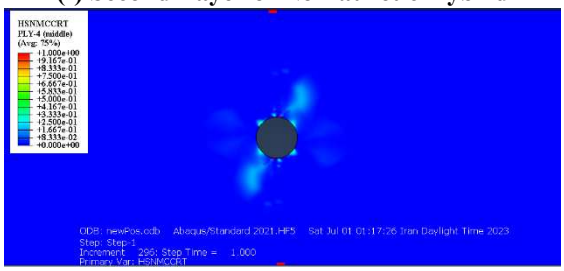


(c) Third Layer of Auxetic Hybrid

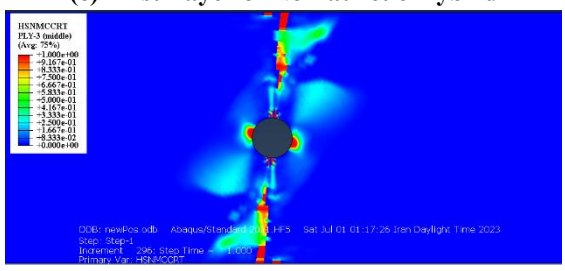




(f) Second Layer of Non-auxetic Hybrid



(e) First Layer of Non-auxetic Hybrid



(h) Fourth Layer of Non-auxetic Hybrid

(g) Third Layer of Non-auxetic Hybrid

Figure 11: Damage Propagation in Matrix Compressive Failure Mode (HSNMCCRT)

Based on the results obtained from Figures 4 to 11, the damage initiation can be categorized by the displacement value at the moment the first element is damaged, as summarized in Table 6.

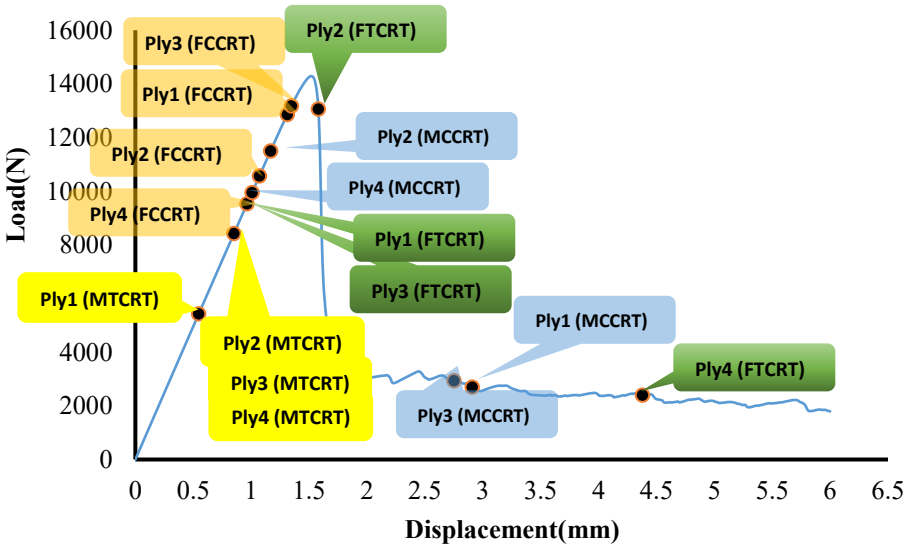
Table 6: Classification of Displacement Values at Damage Initiation for Different Failure Modes

			Displacement At Damage Initiation For Different Failure Modes (mm)			
	Layer Number	**Layer Angle**	**Fibers under Tension**	**Fibers under Compression**	**Matrix under Tension**	**Matrix under Compression**
Hybrid 8-layer with Negative Poisson's Ratio	1	10	0.96	1.31	0.54	2.91
	2	80	1.58	1.07	0.85	1.16
	3	10	0.96	1.34	0.85	2.75
	4	70	4.38	0.96	0.85	1.00
Hybrid 8-layer with Positive Poisson's Ratio	1	10	0.99	1.70	0.99	1.67
	2	45	1.53	1.17	0.99	1.70
	3	-45	1.17	1.69	1.12	1.67
	4	90	1.67	0.99	1.12	1.71

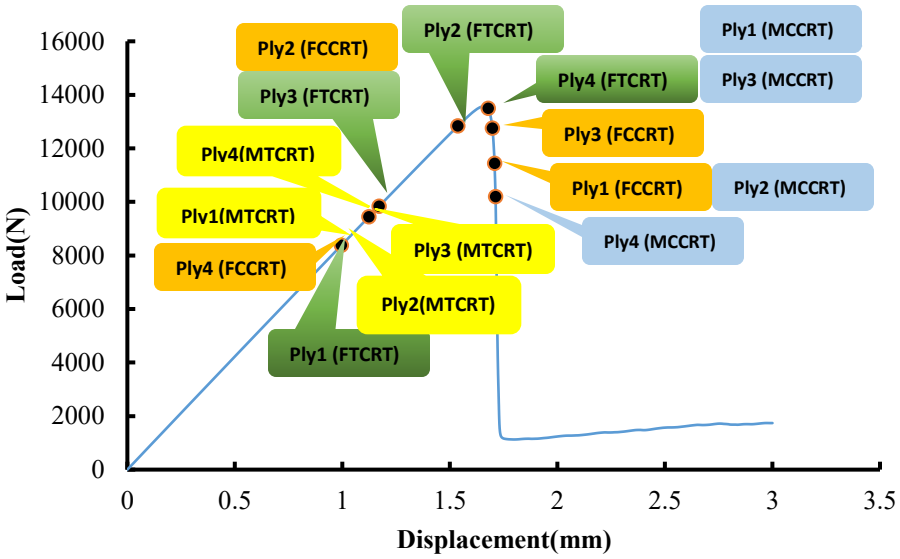
According to Table 6, the first failure mode to initiate in both eight-layer hybrid laminates is matrix cracking under tensile loading. This is entirely expected, given the relatively low strength of the epoxy resin compared to the glass and carbon fibers. In the fiber tensile failure mode, the auxetic laminate experiences initial failure in the 10-degree carbon and glass fiber layers, while in the positive Poisson's ratio laminate, damage begins in the 10-degree carbon fiber layer. For the fiber compressive failure mode in the auxetic laminate, failure initiates first in the 70- degree carbon fiber layer. The same carbon layer also initiates failure in the matrix compressive failure mode. In the fiber compressive failure mode of the positive Poisson's ratio laminate, the 90-degree carbon fiber layer is the first to initiate damage. As mentioned earlier, in the matrix tensile failure mode, damage starts at the first layer in the auxetic laminate, whereas it begins in both the first and second layers in the positive Poisson's ratio laminate. However, failure initiates in other layers shortly thereafter. Examining the damage initiation across the laminates reveals that, in most layers, failure begins near the hole and propagates rapidly. Figure 12 illustrates the damage initiation sites in each layer of the auxetic and positive Poisson's ratio laminates under different failure modes. In most

layers of the non-auxetic laminate, damage initiates before the maximum load is reached, leading to a sudden loss of load-bearing capacity. The positive Poisson's ratio laminate retains less than 10% of its ultimate load after the critical load, whereas the auxetic laminate retains approximately 20%. These percentages represent the remaining load relative to the respective peak load at the post-peak stage shown in the corresponding load–displacement curves. The initial damage occurs at approximately 5428 N in the auxetic laminate and 8376 N in the positive Poisson's ratio laminate. The displacement corresponding to the critical load is about 1.51 mm for the auxetic laminate and approximately 1.65 mm for the positive Poisson's ratio laminate.

Although the auxetic laminate exhibits earlier damage initiation, the subsequent damage progression is more gradual, resulting in improved post-peak load sustainability. Its progressive damage redistribution delays catastrophic collapse. This earlier damage onset represents a trade-off associated with the auxetic configuration. Figure 12 also displays the sequence of damage initiation along with the corresponding load and displacement values for both the auxetic and positive Poisson's ratio laminates.



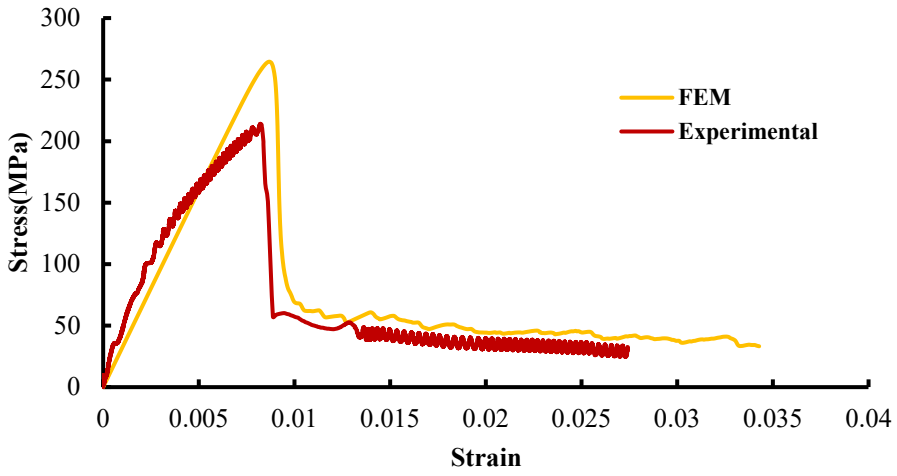
(a)



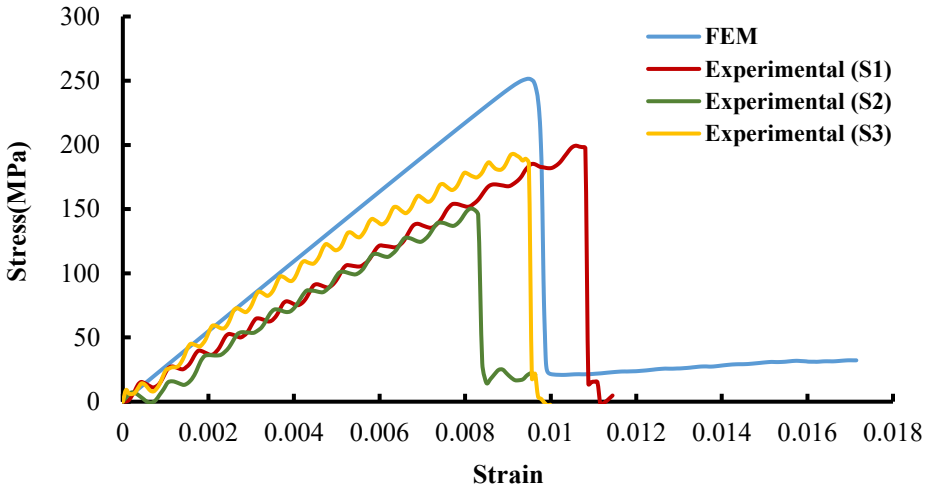
(b)

Figure 12: Load-Displacement Curve and Damage Initiation Visualization in Different Failure Modes with Corresponding Load Values for (a) Auxetic Hybrid Perforated Laminate and (b) Non-auxetic Hybrid Perforated Laminate

Based on the results presented in Figure 13, the peak stress for the auxetic laminate is found to be 214 MPa experimentally and 264 MPa through finite element analysis (FEM). For the Positive Poisson's ratio laminate, this value is 199 MPa experimentally and 251 MPa via FEM. The simulation error for laminates with positive and negative Poisson's ratios is approximately 26% and 23%, respectively. The experimentally measured peak stress of the auxetic laminate was approximately 7.5% higher than that of the positive Poisson's ratio laminate in the present tests. However, this difference should be interpreted cautiously because of the limited number of specimens and the absence of statistical significance analysis. Although further mesh refinement may slightly reduce the numerical error, the discrepancy is primarily attributed to interlaminar delamination and manufacturing-induced imperfections, which are not explicitly captured in the current intralaminar damage model. Accordingly, a mesh containing 10,800 elements was adopted for all subsequent simulations. Moreover, improving critical factors such as manufacturing conditions, sample cutting methods, testing device accuracy, and computational errors could further decrease the discrepancy. The experimentally tested specimens reached critical failure at lower stress levels than predicted by the numerical simulations, primarily due to edge-induced microcracks and interlaminar delamination effects. The propagation of these defects during loading also causes nonlinearity in the stress-strain curve, which is clearly observable in the plot of Figure 13.



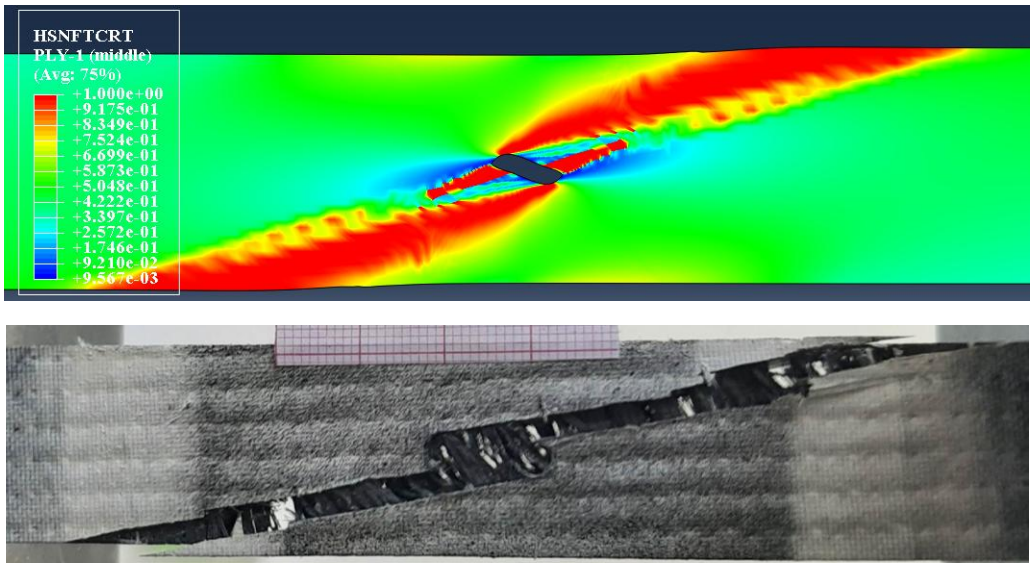
(a) Auxtic Perforated Hybrid Multilayer



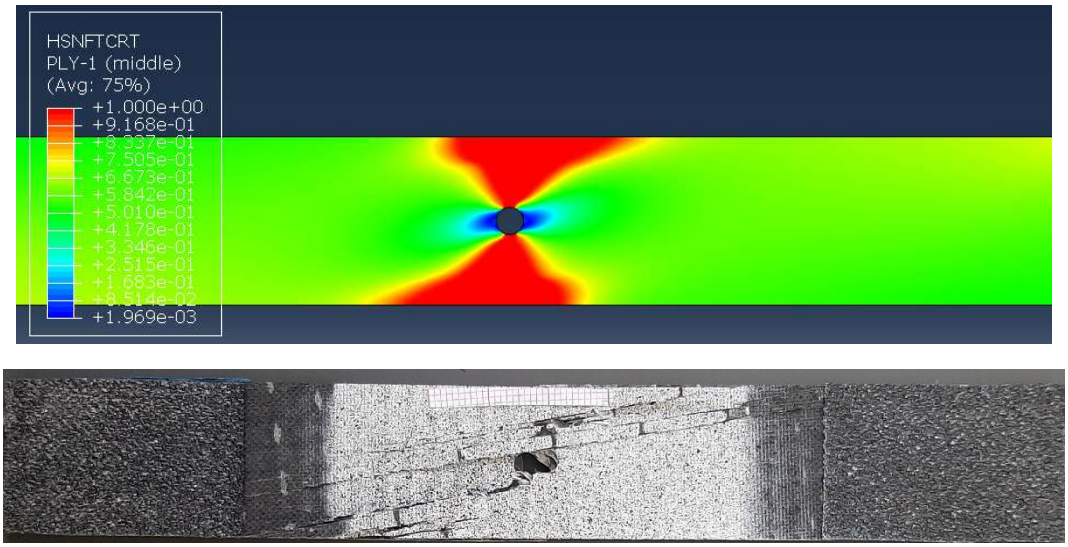
(b) Non-auxetic Perforated Hybrid Multilayer

Figure 13: Comparison of experimental and numerical stress–strain responses for the auxetic laminate and the conventional laminate

To assess the ability of the numerical model to reproduce the expected fracture behavior of orthotropic laminates, the predicted fiber tensile damage path in the first ply was compared with the experimentally observed fracture pattern. As shown in Figure 14, damage initiates near the hole and propagates approximately along the dominant fiber orientation in both laminate configurations. The predicted fracture angle, propagation direction, and damaged region are in reasonable qualitative agreement with the experimental observations. This comparison confirms that the adopted Hashin-based formulation can reproduce the principal intralaminar failure path, although interlaminar delamination is not explicitly represented in the present shell-based model.



(a)



(b)

Figure 14: Comparison of Fiber Failure in the First Layer under Tensile Loading with Experimental Test Results for (a) Auxetic Hybrid and (b) Non-auxetic Hybrid

Furthermore, examination of the tested specimen in the laboratory reveals that, in addition to the four failure modes analyzed in the finite element method, these laminates also exhibit interlaminar delamination. It should be emphasized that the present numerical model is limited to intralaminar damage mechanisms and does not explicitly account for interlaminar cohesive behavior. Reviewing the recorded test footage shows that the significant difference in fiber orientation angles between adjacent layers in the negative Poisson's ratio laminate has made this failure mode more pronounced. Additionally, the use of lower epoxy content during specimen fabrication (resulting in a higher fiber volume fraction) leads to weaker bonding between the laminate plies, making

delamination more likely to occur. Figure 15 illustrates the interlaminar delamination observed in the negative Poisson's ratio specimen.

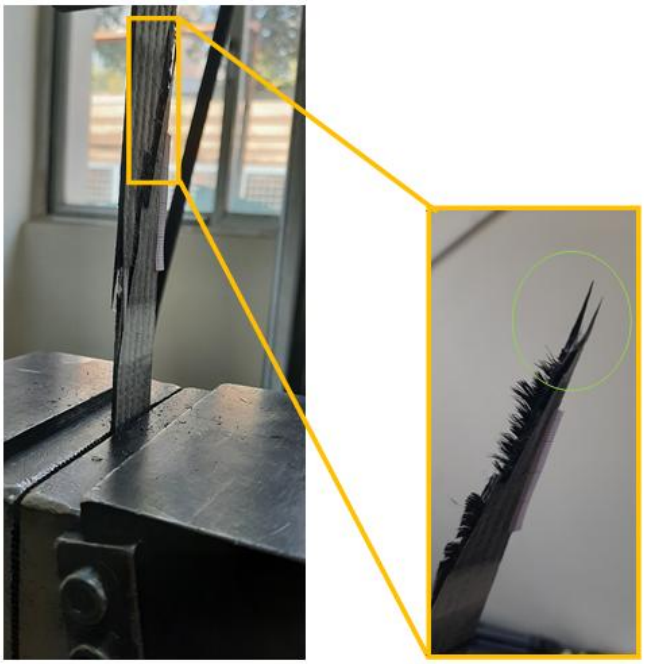


Figure 15: Interlaminar Delamination in Eight-Layer Hybrid with Negative Poisson's Ratio

Conclusion

This study systematically investigated the damage initiation and propagation mechanisms in perforated hybrid composite laminates with negative (auxetic) and positive Poisson's ratios through a combined experimental and finite element approach. By maintaining identical constituent material systems, nominal fiber volume fraction, laminate thickness, and carbon/glass ply distribution while varying only the ply orientation sequence, the isolated influence of auxetic layup design on structural damage behavior was rigorously evaluated. The results demonstrate that although auxetic laminates experience earlier damage initiation in certain failure modes primarily matrix tensile cracking the subsequent damage evolution is more controlled and spatially distributed compared to positive Poisson's ratio laminates. This redistribution of stresses around the hole reduces abrupt stress concentration and delays catastrophic structural collapse. Consequently, auxetic laminates retain approximately 20% of their peak load after the onset of catastrophic failure, whereas positive Poisson's ratio laminates exhibit a sharp load drop and preserve less than 10% of their residual strength. At the laminate level, failure initiation in auxetic configurations predominantly occurs in low-angle plies (e.g., 10°) and intermediate-angle plies (around 70°), followed by progressive and relatively uniform damage propagation due to the symmetric and mechanically balanced stacking sequence. In contrast, positive Poisson's ratio laminates show damage concentration in 90° plies, leading to rapid cross-sectional failure and reduced structural tolerance. The comparison between experimental observations and Hashin-based finite element simulations revealed reasonable agreement in terms of failure patterns,

fracture angles, and damage localization, despite quantitative discrepancies in peak stress prediction. The observed deviations are mainly attributed to interlaminar delamination and manufacturing-induced imperfections, which were not explicitly modeled in the current framework. From an engineering perspective, the findings indicate that incorporating auxetic layup strategies in perforated hybrid composites can enhance post-critical load sustainability and mitigate sudden structural collapse, making them promising candidates for lightweight load-bearing composite structures containing stress concentrators, such as mechanically fastened joints, cut-outs, and other perforated structural components. However, the study also identified limitations associated with increased susceptibility to interlaminar delamination due to large ply angle mismatches. Future work should incorporate cohesive zone modeling to capture interlaminar damage, extend the analysis to three-dimensional stress states, and evaluate energy absorption capacity under impact or cyclic loading conditions to further clarify the structural advantages of auxetic hybrid laminates.

CRediT authorship contribution statement

Hossein Hosseini-Toudeshky: Supervision, Writing–review & editing; Sina Esmaeili Yengejeh: Software; Validation; Writing–original draft; Methodology; Investigation; Data curation; Azizollah Navaei: Conceptualization; Investigation; Validation; Software, Writing–review & editing

All authors approved the final version.

Funding Declaration

The authors received no financial support for this article.

Declaration of competing interest

The authors declare that they have no known competing financial interests or personal relationships that could have appeared to influence the work reported in this paper.

Data availability

Data will be made available on request.

References

[1] Dalfi, H. K., Jan, K., Yousaf, Z., et al. Improving the impact resistance and damage tolerance of fibre reinforced composites: a review. Journal of Composite Materials, 57(28), 4479–4500 (2023).

[2] Monticeli, F. M., Fuga, F. R., Arbelo, M. A., et al. The effect of fibre orientation on fatigue crack propagation in CFRP: finite fracture mechanics modelling for open-hole configuration. Engineering Failure Analysis, 161, 108278 (2024).

[3] Harkati, A., Chouai, S., Harkati, E. H., et al. Using a negative Poisson's ratio to mitigate stress concentrations in perforated composite plates. Physica Status Solidi B, 261, 2400115 (2024).
[4] Chen, Y., He, Q. 3D-printed short carbon fibre reinforced perforated structures with negative Poisson's ratios: mechanisms and design. Composite Structures, 236, 111859 (2020).
[5] Danzi F, Tavares RP, Xavier J, et al. Effects of hybridization and ply thickness on the strength and toughness of composite laminates. *Journal of Composite Materials* 2021;55(30):4601–4616.
[6] Uppin VS, Gouda PS, Sridhar I, et al. Glass-carbon hybrid veil interleaving to enhance fracture toughness and shear strength in glass epoxy composites: an experimental study. *Theoretical and Applied Fracture Mechanics* 2025;139:105075.
[7] Rahimian Koloor SS, Karimzadeh A, Yidris N, et al. An energy-based concept for yielding of multidirectional FRP composite structures. *Polymers* 2020;12:157.
[8] Bruno M, Carrino L, Donadio F, et al. Damage analysis of hybrid composites under multi-impact loads. *Key Engineering Materials* 2022;926:1939–1948.
[9] Parente J, Ferreira LM, Reis PN. Damage mechanisms in hybrid composites: experimental characterisation and energy-based numerical analysis. *Frattura ed Integrità Strutturale* 2025;19:139–152.
[10] Herakovich CT. Composite laminates with negative through-the-thickness Poisson's ratios. *Journal of Composite Materials* 1984;18:447–455.
[11] Zhang R, Yeh HL, Yeh HY. A preliminary study of negative Poisson's ratio of laminated fiber reinforced composites. *Journal of Reinforced Plastics and Composites* 1998;17:1651–1664.
[12] Zhang R, Yeh HL, Yeh HY. A discussion of negative Poisson's ratio design for composites. *Journal of Reinforced Plastics and Composites* 1999;18:1546–1556.
[13] Hosseini-Toudeshky, H., Esmaeili Yengejeh, S., Navaei, A. Effects of layups with negative and positive Poisson's ratios on the stress–strain behaviors of plain and holed hybrid composite laminates. *Journal of Reinforced Plastics and Composites*, 45, 1406–1421 (2026).
[14] Harkati, E. L. H., Bezazi, A., Scarpa, F., et al. Modelling the influence of orientation and fibre reinforcement on negative Poisson's ratio. *Physica Status Solidi B*, 244, 883–892 (2007).
[15] Lin, W., Wang, Y., Davidson, B. D. Negative Poisson's ratio can enhance stability of layered composite structures. *Thin-Walled Structures*, 205, 112409 (2024).
[16] Jiang, H., Xiao, S., Yang, Y., et al. Reinforced structural design, additive manufacturing and crashworthiness of continuous fiber reinforced composite negative Poisson's ratio honeycomb. *Thin-Walled Structures*, 206, 114190 (2025).
[17] Veloso, C., Mota, C., Cunha, F., et al. Evaluation of tensile properties in in-plane auxetic carbon/epoxy and carbon–glass/epoxy composite laminates. *Journal of Composite Materials*, 59, 2073–2085 (2025).
[18] Wang, Y. Auxetic composite laminates with through-thickness negative Poisson's ratio for mitigating low velocity impact damage. *Materials*, 15, 6963 (2022).
[19] Saremian, R., Jamal-Omidi, M., Pirkandi, J. Numerical investigation on auxetic angle-ply CFRP laminates under low-velocity impact loading. *Archive of Applied Mechanics*, 94, 3625–3646 (2024).

[20] Saremian, R., Jamal-Omidi, M., Pirkandi, J., et al. A numerical study on the low-velocity impact resistance and damage behavior of auxetic CFRP laminated cylinders. *Mechanics of Advanced Materials and Structures*, 32, 1–16 (2025).
[21] Usta, F., Türkmen, H. S., Scarpa, F. Low-velocity impact resistance of composite sandwich panels with auxetic and non-auxetic core structures. *Thin-Walled Structures*, 163, 107738 (2021).
[22] Steffens, F., Oliveira, F. R., Fangueiro, R. Energy absorption from composite reinforced with high-performance auxetic textile structure. *Journal of Composite Materials*, 55, 1003–1013 (2020).
[23] Li, T., Chen, Y., Hu, X., et al. Exploiting negative Poisson's ratio to design 3D-printed composites. *Materials & Design*, 142, 247–258 (2018).
[24] Chen, Y., Ye, L. Designing and tailoring negative Poisson's ratio with continuous carbon fibres using 3D printing. *Composites Part A: Applied Science and Manufacturing*, 150, 106625 (2021).
[25] Etemadi, E., Zhang, M., Gholikord, M., et al. Quasi-static and dynamic behavior analysis of 3D CFRP woven laminated composite auxetic structures for load-bearing and energy absorption applications. *Composite Structures*, 340, 118182 (2024).
[26] Kumar, P., Meena, A., Mulay, S. S. Numerical modeling of three-dimensional quasi-brittle fracture and machining-induced damage in orthotropic composites. *Theoretical and Applied Fracture Mechanics*, 140, 105415 (2025).
[27] Neesu, V. M. K., Pandey, V. B., Mahajan, P., et al. Efficient analytical modeling of progressive damage and contact stiffening in composite laminate under repeated impacts. *Composite Structures*, 355, 120138 (2026).
[28] Nguyen, M. H., Waas, A. M. A novel mode-dependent and probabilistic semi-discrete damage model for progressive failure analysis of composite laminates – Part II: applications to unnotched and open-hole tensile specimens. *Composites Part C: Open Access*, 3, 100071 (2020).
[29] Hosseini-Toudeshky, H., Navaei, A. Characterization of elastic modulus at glass/fiber interphase using DIC and FEM. *Mechanics of Advanced Materials and Structures*, 31, 6126–6138 (2024).
[30] Gljušćić, M., Franulović, M., Lanc, D., et al. Application of digital image correlation in behavior modelling of AM CFRTP composites. *Engineering Failure Analysis*, 136, 106133 (2022).
[31] Xu, D., Cerbu, C., Wang, H., et al. Hybrid composite materials considering DIC measurements. *Mechanics of Materials*, 135, 46–56 (2019).
[32] Cardoso, D., Pereira, R., Moura, M., et al. Assessment of fracture process zone length in carbon fiber-reinforced epoxy composites through digital image correlation. *Theoretical and Applied Fracture Mechanics*, 136, 104816 (2025).
[33] Pourabdollah, V., Haji Aboutalebi, F., Beheshti, H., et al. Comparison of three composite failure criteria using airfoil loading test. *Mechanical Engineering*, 48, 55–64 (2018).
[34] Hashin, Z. Failure criteria for unidirectional fiber composites. *Journal of Applied Mechanics*, 47, 329–334 (1980).
[35] Dassault Systèmes. *Abaqus Analysis User's Manual*. Version 2021. Providence, RI, USA: Dassault Systèmes Simulia Corp.; 2021.
[36] Lapczyk, I., Hurtado, J. A. Progressive damage modeling in fiber-reinforced materials. *Composites Part A: Applied Science and Manufacturing*, 38, 2333–2341 (2007).

[37] Hosseini-Toudeshky, H., Sheibanian, F., Fazlali, B., Mohammadi, B. Progressive damage analysis of open holed cross-ply laminate under static loading. In: *The 6th International Conference on Composites: Characterization, Fabrication, and Applications* (2018). Available at: https://civilica.com/doc/901588.
[38] Abdalla, H. M. A. Review of rules of mixture for effective elastic properties in fibrous and particulate composite materials. *Composite Structures*, 367, 119216 (2025).
[39] Halpin, J. C., Kardos, J. L. The Halpin-Tsai equations: A review. *Polymer Engineering & Science*, 16(5), 344–352 (1976).